

Received: 24 February, 2025

Accepted: 07 March, 2025

Published: 08 March, 2025

***Corresponding author:** MJ Birch, Jeremiah Horrocks Institute for Mathematics, Physics and Astronomy, University of Central Lancashire, Preston, UK, E-mail: mjbirch@uclan.ac.uk

ORCID: <https://orcid.org/0009-0009-4578-9248>

Keywords: Coronal hole; Wind spacecraft; ACE spacecraft; Particle flux

Copyright License: © 2025 Birch MJ. This is an open-access article distributed under the terms of the Creative Commons Attribution License, which permits unrestricted use, distribution, and reproduction in any medium, provided the original author and source are credited.

<https://www.mathematicsgroup.us>



Review Article

On the Determination of the Speed of a Fast Solar Wind Stream Using Two Independent Measurements of the Interplanetary Magnetic Field

MJ Birch*

Jeremiah Horrocks Institute for Mathematics, Physics and Astronomy, University of Central Lancashire, Preston, UK

Abstract

The fast solar wind stream which resulted from the helio-meridional crossing of an equatorial coronal hole on June 29th and 30th 2005 passed the Wind and Advanced Composition Explorer (ACE) spacecraft during July 1st and 2nd. This fast stream caused a moderate magnetospheric storm following a weak (though clearly defined) sudden commencement at 14:12 UT on July 1st. During the event, the two spacecraft were both in the vicinity of the L1 libration point, though separated in the Sun-Earth direction by about 150000 km. An algebraic method is described whereby the speed of the particle flux can be determined using measurements of the interplanetary magnetic field at the two spacecraft.

Introduction

Scientific study of the solar wind first began with the work of S. Chapman and V.C.A. Ferraro [1-3], who suggested that it comprises streams of 'corpuscles' ejected by the Sun, which reach the Earth a day or so later. Biermann [4] studied comet tails and concluded that electromagnetic radiation pressure was insufficient to account for the observations, that the stream of corpuscles actually comprised particles, that it was continually present, and that the velocity was about 500 km.s⁻¹ (a surprisingly good estimate). Subsequent studies by Parker [5] and Chapman & Aller [6] proved that, unlike the Earth's atmosphere, the solar corona is not in hydrostatic equilibrium but instead expands continually, with matter streaming out into the heliosphere in the form of *solar wind*.

The continuity of the solar wind was firmly established by Mariner-2 during its flight to Venus in 1962 when it recorded alternating dense, low-speed (300 - 500 km.s⁻¹) and tenuous high-speed (500 - 800 km.s⁻¹) streams [7]. This finally confirmed that the solar wind is a permanent feature

of the solar system. Ulysses, launched in 1990 to measure the Interplanetary Magnetic Field (IMF) between 1.35 and 5.4 AU, was the first spacecraft to measure the solar wind at all heliolatitudes. It was also the first to confirm that the solar wind is bimodal in nature, having slow and fast components [8].

It is now well known that the fast solar wind emerges primarily from coronal holes and expands to fill the majority of the heliospheric volume with speeds from 450 to 900 km.s⁻¹ [9-11], whereas the slow component (250 to 450 km.s⁻¹) is associated with coronal streamers [12,13] and may also have contributions arising from boundary flow along current sheets, the magnetic reconnection of closed-field loops, and the boundaries of coronal holes [14]. The passage of low-latitude coronal holes across the helio-meridian often results in weak to moderate magnetic storms within the geospace [15,16] the intensity being mainly dependent on the orientation of the IMF and the dynamic pressure of the solar wind.

Following solar maximum, the coronal holes which are prevalent at the poles begin to extend towards equatorial

latitudes, sometimes crossing the helio-equator. At solar minimum, the high-speed wind dominates at high latitudes, while the low-speed component coexists at lower latitudes with occasional high-speed streams. Low-latitude coronal holes are therefore most evident during the declining years of sunspot activity following solar maximum and before solar minimum.

A typical fast solar wind stream from a low-latitude coronal hole has a compression region (or co-rotating interaction region [17] on the leading edge (which may have an associated shock front) and a rarefaction region on the trailing edge. In terms of geospace effects, the co-rotating interaction region is the dominant component of a fast solar wind stream, though the strength and duration of the southward component of the interplanetary magnetic field, the strength of the solar wind pressure pulse, and the prior state of the magnetosphere are also significant factors affecting geo-effectiveness [18].

In 2005, as solar activity declined toward the minimum, the solar wind was dominated by fast streams emanating from recurrent equatorial coronal holes. The solar particle event under consideration occurred during this period and resulted from the heliomeridional passage across the solar disc by a coronal hole (Figure 1) which induced a moderate geomagnetic storm during July 1 and 2. This was the largest equatorial coronal hole to emerge since the 'Elephant's Trunk' of summer 1996 [19].

This study uses data from the ACE [20,21] and Wind [22,23] spacecraft, both located in the vicinity of the L1 libration point. (Though tasked to study the magnetosphere and the Lunar environment during the first phase of its mission, Wind has been continually in the vicinity of L1 since 2004.) During the period of observation, Wind and ACE were positioned slightly above the ecliptic, on either side of the Sun-Earth line in the XY GSE plane. The configuration is shown in relation to Earth and L1 in Figure 2, and in more detail with respect to L1 in Figure 3.

In this paper, an algebraic method is described whereby the velocity of the particle flux of the fast solar wind stream can be determined by measuring the interplanetary magnetic field at the Wind and ACE spacecraft, without recourse to a particle detector. A detailed error analysis is provided, and the application of the method to other spacecraft geometries is discussed.

Description of the event at L1.

The leading edge of the coronal hole (Figure 1) first crossed the helio-meridian on June 29 2005 at about 00:00 UT (± 3 hours, the edge being somewhat difficult to discern precisely). The ACE real-time summary plot gives an overview of the complete event over about 6 days (Figure 4). Before the event, quiescent conditions prevailed, typical of the slow solar wind: the density varied from 1 to 3 cm^{-3} (panel 'c'), the speed was steady at $\approx 400 \text{ km.s}^{-1}$ (panel 'd'), and B_z was limited to oscillations within $\approx \pm 5 \text{ nT}$ (red plot, panel 'a').

The first clear evidence for the arrival of the co-rotating interaction region can be seen on July 1 at about 13:20 UT: an abrupt increase in density to $\approx 30 \text{ cm}^{-3}$, the start of a gradual

increase in speed, an enhancement in B_z , and strong oscillations in B_z . (Though there is a brief data gap in ACE density at the arrival time of the compression region, the velocity data (not shown) gives an estimate of 13:20 UT.)

The interval of maximum activity lasted from 13:20 UT on July 1 to about 06:00 UT on July 2: strong oscillations in B_z (with southerly excursions to $\approx -12 \text{ nT}$ at 15:30, 17:30, and 21:30

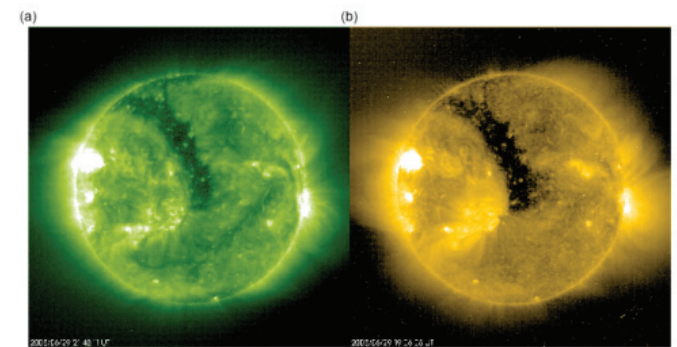


Figure 1: Images of the Sun from the EIT instrument aboard the SOHO spacecraft at L1, June 29, 2005: (a) 195 Å at 21:48 UT; (b) 284 Å at 19:06 UT.

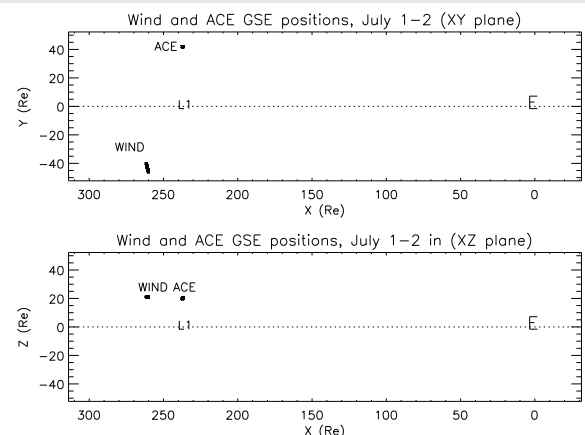


Figure 2: The geometry of Wind and ACE in the vicinity of Earth (E) and L1 during the event.

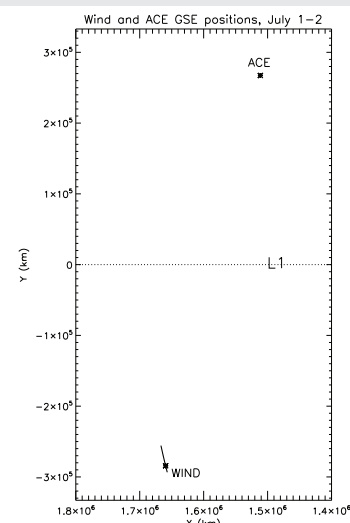


Figure 3: The detailed geometry of Wind and ACE in the vicinity of L1 during the event (the mean separation in X is 151200 km).

UT, each of duration 1 to 2 hours); an enhancement in B_t to ≈ 18 nT; an abrupt increase in speed to ≈ 650 km.s⁻¹; and a gradual reduction in density to ≈ 5 cm⁻³.

After 06:00 UT on July 2, over a recovery period that lasted more than 4 days, the solar wind gradually returned to behaviour characteristic of the slow component: the speed decreased gradually to about 400 km.s⁻¹, and B_z , B_t , and density returned to their pre-event levels.

Figure 5 shows in greater detail the variations in B_z , P_{dyn} , and bulk speed at the Wind spacecraft from 00:00 UT on July 1 to 12:00 UT on July 2, the most active period. Of particular interest is the abrupt increase in dynamic pressure (panel 'b') at 13:00 UT (dashed line) resulting from the order of magnitude increase in density at that time. It is likely that this dynamic pressure pulse caused the weak sudden commencement recorded at 14:12 UT (Figure 6) by the ground-based magnetometers at Shigaraki (34.8° N, 136.1° W), Urumqi (43.8° N, 87.7° W), and Kakioka (36.2° N, 140.2° W). The 'dash-dot' line in Figure 5 indicates the approximate end of the magnetic 'packet' characteristic of the compression region (the significance of the dotted lines will be covered in Section 4).

During the interval from 15:00 UT on July 1st to 03:00 UT on July 2nd the average K_p index increased to 4, indicating moderate storm conditions. Throughout this interval, solar wind density, speed, and temperature were markedly enhanced, and B_z showed its strongest southerly oscillations.

This was a particularly 'clean' event; no other significant geoeffective solar activity from X-ray flares or CMEs was observed throughout the period of fast solar wind resulting from the meridian passage of the coronal hole. This lack of transient activity, and the gradual 'arch' shape of the coronal hole as it extends northwards from the helio-equator, probably explain the remarkably linear decline in solar wind speed during the recovery phase of the event.

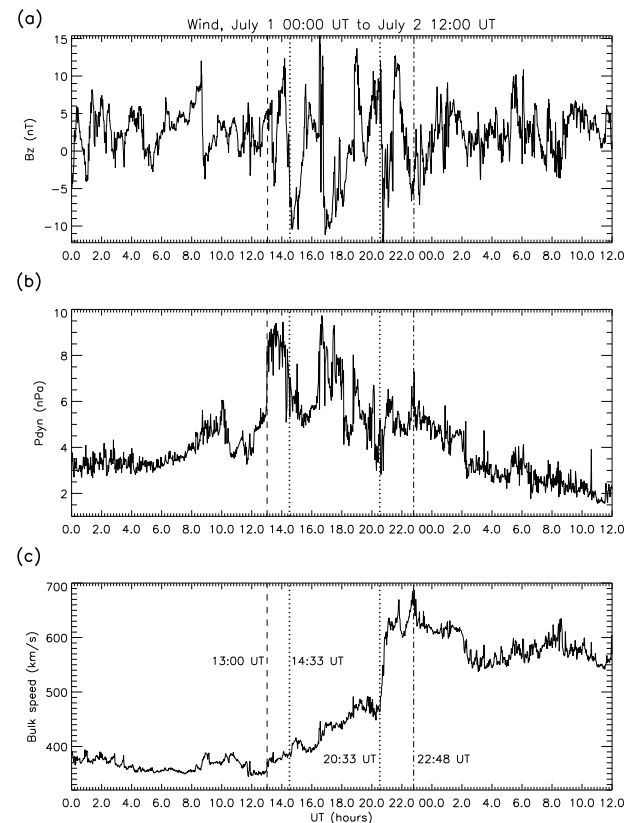


Figure 5: Wind observations from 00:00 UT on July 1 to 12:00 UT on July 2 (1 min. data): (a) IMF B_z (nT); (b) SW dynamic pressure (nPa); (c) SW bulk speed (km/s). (The dashed line marks the start of the event, the dotted lines mark the interval of optimum correlation of B_z and the dot-dash line marks the approximate end of the event.)

Delays in the IMF between Wind and ACE using selected features

The average solar wind speed from the Sun to the Earth can be estimated by dividing the total distance ($1.52e + 08$ km) by the difference between the time at which the leading edge of the coronal hole first crossed the helio-meridian (00:00 UT on June 29th) and the time at which the sudden commencement occurred (14:12 UT on July 1st). This gives 679 ± 32 km.s⁻¹, the main uncertainty being in the estimate of the helio-meridian crossing (± 3 hours).

Alternatively, the average speed can be estimated by dividing the distance from the Sun to L1 by the difference between the time of the helio-meridian crossing (the same as above) and the time that the event was first detected at L1 (by using the leading edge of the dynamic pressure pulse, at about 13:00 UT at Wind). This method gives a velocity of 685 ± 32 km.s⁻¹, the time of the helio-meridian crossing once again being the dominant uncertainty in this estimate. However, these estimates give only the average speed over the total distance from the Sun, and we require the speed at L1, without recourse to a particle detector.

The IMF measurements from both Wind and ACE are clearly similar for this event (Figures 7,8). (As will subsequently be seen, it is the coherent nature of the two independent time series of N/S magnetic flux density (B_z) that enables the

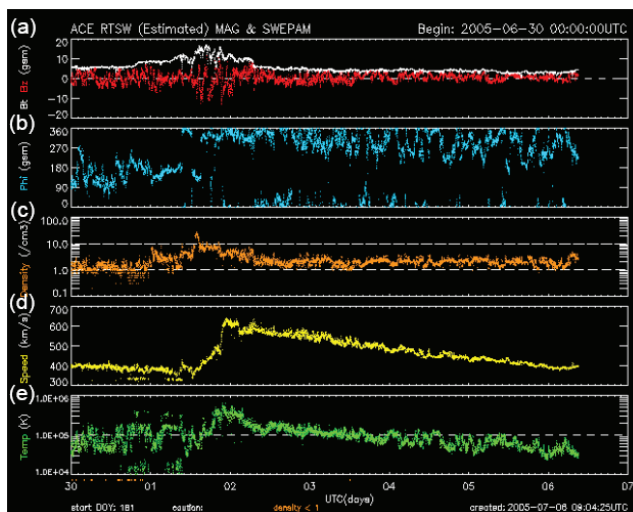


Figure 4: Real-time ACE plots of the solar wind environment at the L1 libration point from June 30 to July 6, 2005: (red) IMF B_z (nT); (white) IMF B_t (nT); (blue) IMF clock angle (degrees); (orange) solar wind density (cm⁻³); (yellow) solar wind speed (km.s⁻¹); (green) solar wind temperature (°K). (Courtesy of the ACE Science Centre, California Institute of Technology.)

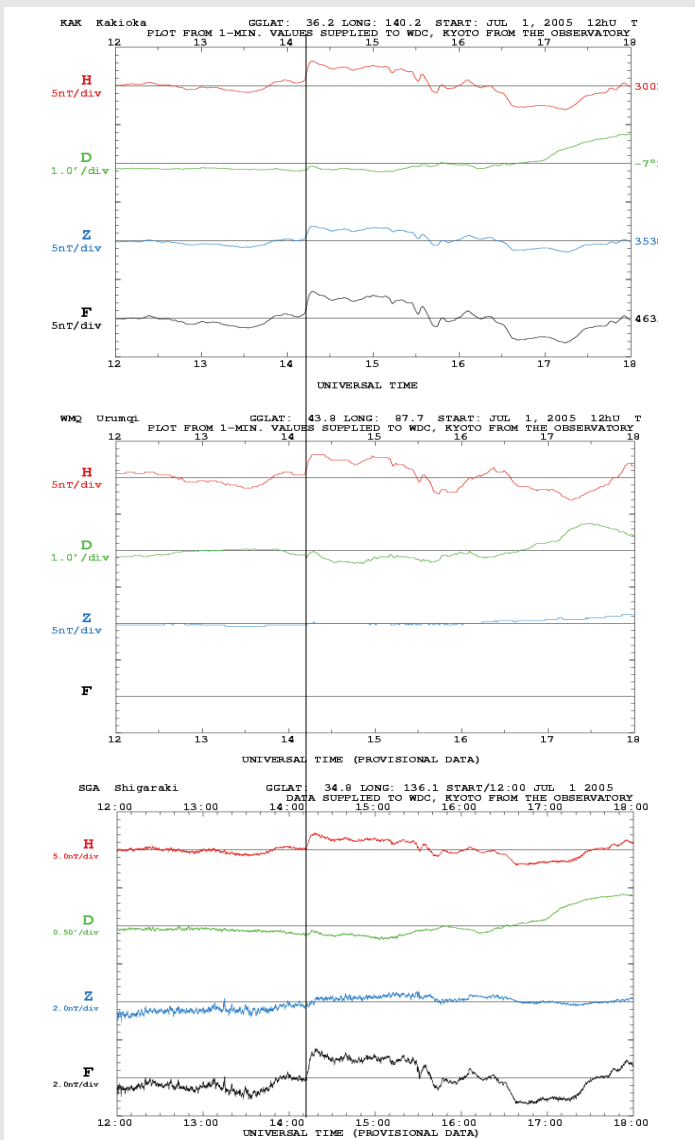


Figure 6: Magnetometer responses to the arrival of the co-rotating interaction region at the magnetopause on July 1st, at Kakioka, Urumqi, and Shigaraki. The vertical line marks the sudden commencement at 14:12 UT.

determination of the solar wind speed.) Using for comparison five clearly identifiable features in the IMF (three sector boundary changes in B_x and B_y , and two significant spikes in B_z), five delay times were measured: (ACE, Wind) = (9.36, 8.71), (12.51, 11.76), (15.16, 14.64), (17.11, 16.57) and (18.35, 17.85) hours. These measurements (taken from 1-minute data files) give delays of 39, 45, 31, 32, and 30 minutes, giving a mean of 35 minutes with a standard deviation of 6 minutes.

Clearly, the delays derived from these spot values vary considerably and are not reliable measures. Consequently, a running cross-correlation was performed on the Wind and ACE IMF data in order to determine a delay that is free from the variations necessarily associated with point-to-point selections.

Correlation of B_z at Wind and ACE during the event

Wind and ACE 1-second B_z time series were used in these

correlation tests (the analysis soon revealed that B_x , B_y , and B_z gave very poor results). A lagged cross-correlation of the ACE and Wind time series covering the entire event would not have been suitable for determining the delay because the limits of the event and the centre of activity are not defined, and so the result cannot be compared with a measured solar wind speed. Instead, a series of 11 running cross-correlations were carried out on the Wind B_z data from 06:00 UT on July 1 to 06:00 UT on July 2, against successively increasing intervals in ACE B_z data, each centred at 18:00 UT on July 1, and each of duration $\pm n$ hours, where $n = 1.0 \dots 6.0$ in 0.5 hour increments. (Tests with ACE B_z centred from 14:00 to 22:00 UT in 1-hour increments showed a rapid reduction in correlation when the centre diverged from 18:00 UT, proving this to be the mid-point of the IMF activity.)

In the resulting correlograms, as n increases, a distinct peak in the correlation coefficient (ρ) steadily emerges above the background. However, the value of ρ associated with each peak does not increase with n , as can be seen in Figure 9a. In fact, there is a distinct peak for $n = 1.5, 2.0, 2.5$, and 3.0 ($\rho = 0.90, 0.88, 0.87$, and 0.88 , respectively), all of which give a delay of 1610 seconds (Figure 9b), with Wind preceding ACE.

The correlograms for each of these four values of n are shown in Figure 10, in which the peak emerges above the background as the width of the ACE interval increases from $n = 1.5$ to $n = 3.0$. It is considered that the ACE interval defined by $n = 3$ (from 15:00 to 21:00 UT), with $\rho = 0.88$, gives the optimum correlation (the peak is more distinct relative to the

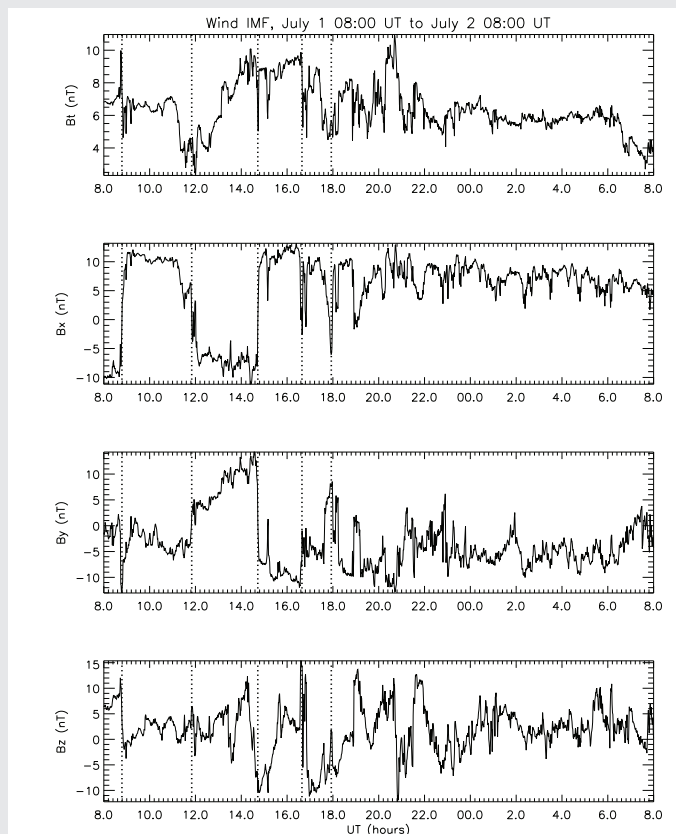


Figure 7: IMF flux density at the Wind spacecraft during July 1st and July 2nd, 2005. (The dotted lines mark the features selected for comparison with ACE in Figure 8.)

background, even though $\rho = 0.90$ when $n = 1.5$). The result is clearly robust because all four values of n give the same delay which, when applied to Wind, gives the optimum interval from 14:33 to 20:33 UT (27 minutes delay, to the nearest minute). These UT limits are marked in Figure 5c as dotted lines.

With a mean separation between Wind and ACE of 149820 km, this 1610-second delay gives a mean solar wind speed of 93.4 km.s^{-1} , which is obviously incorrect, being based on a delay in the *field*, not the *particles*. Consequently, consideration must now be given to the relationship between the solar wind and its embedded magnetic field.

An algebraic model of the field line geometry at L1.

The solar wind speed cannot simply be derived by dividing the separation of Wind and ACE along the Sun-Earth axis by the delay in the field because the particles emanate radially from the Sun as it rotates, but the frozen-in magnetic field is rooted in the photosphere. Any given field line represents the locus of all the particles originating at a single location on the solar surface, forming an Archimedean (or Parker) spiral [5], a curve that in polar coordinates (r, θ) can be described by the equation $r = a + b\theta$. For the solar wind, a represents the solar rotation rate and b the bulk speed (effectively, the speed in the Sun-Earth direction). For example, $b = 250 \text{ (km.s}^{-1}\text{)}$ gives a typical field line with the angle between the spiral and the Sun-Earth line at 1 AU being $\approx 45^\circ$, which is indeed the angle confirmed by observation during periods when this solar wind speed is dominant.

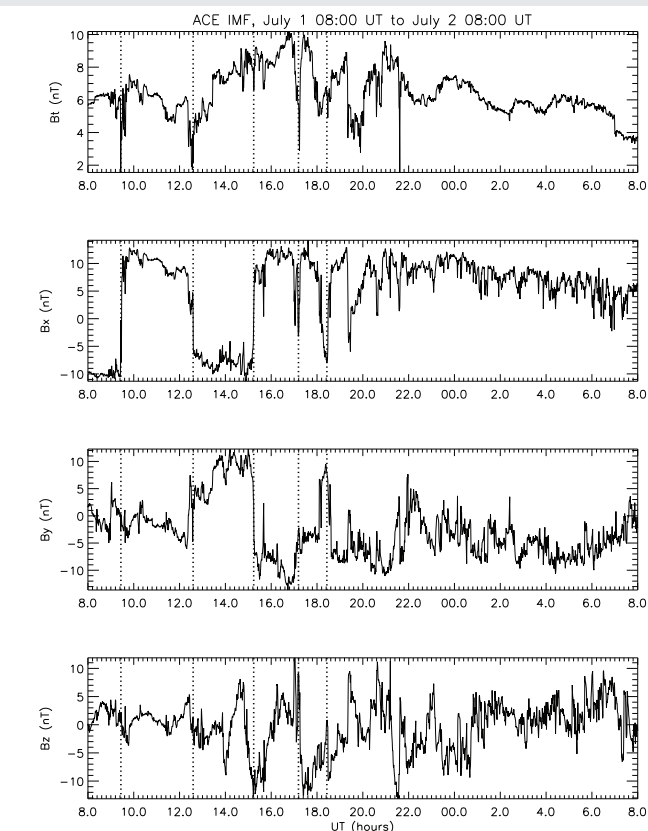


Figure 8: IMF flux density at the ACE spacecraft during July 1st and July 2nd, 2005. (The dotted lines mark the features selected for comparison with Wind in Figure 7.)

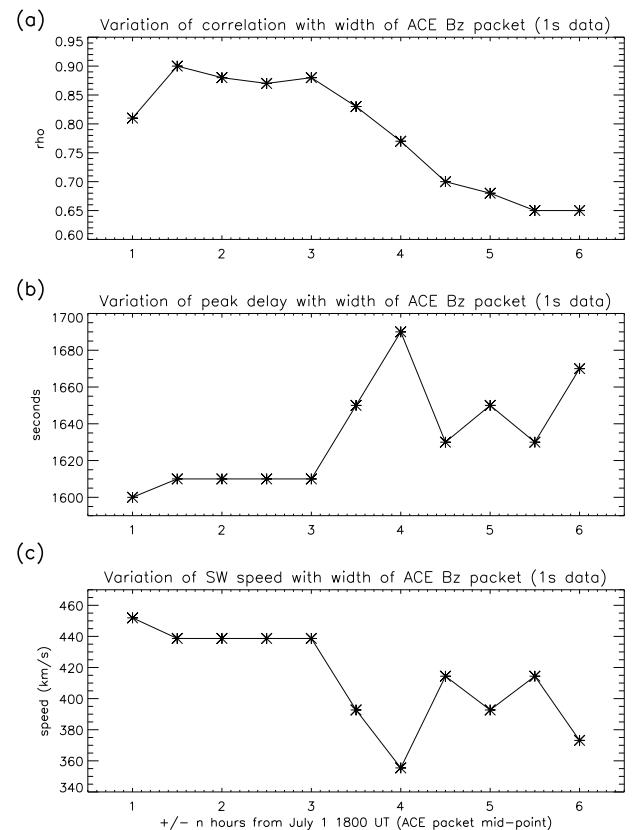


Figure 9: Correlation of Wind B_z against ACE B_z (1 s data), relative to the width of ACE interval: (a) correlation coefficient; (b) peak delay; (c) solar wind speed (deduced from the delay, using the algebraic model).

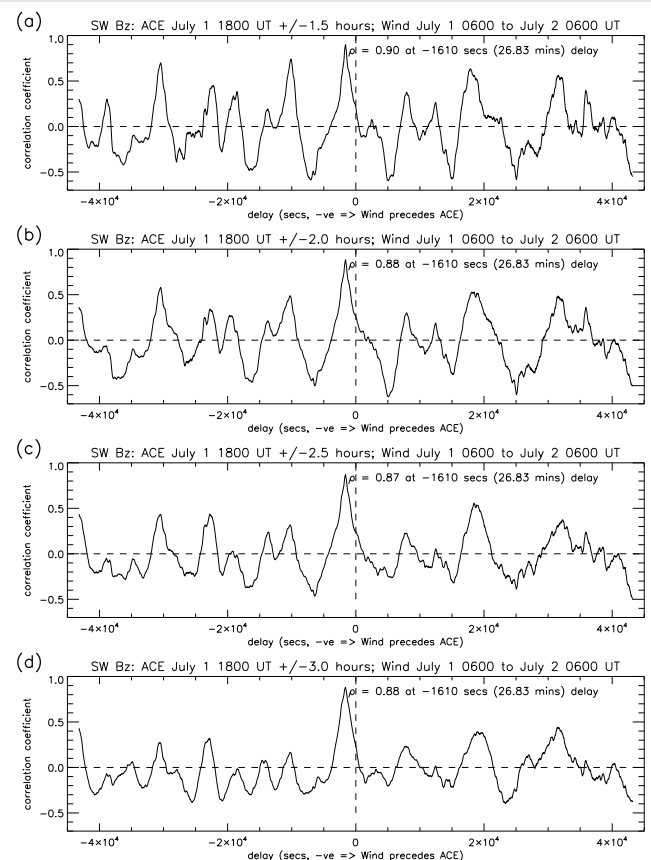


Figure 10: Correlograms of 1-second B_z time series for ACE (on July 1 at 18:00 UT $\pm n$ hours) against Wind (from 06:00 UT on July 1 to 06:00 UT on July 2): (a) $n = 1.5$ hours; (b) $n = 2.0$ hours; (c) $n = 2.5$ hours; (d) $n = 3.0$ hours.

By demonstrating how the process of field line growth in the vicinity of L1 is related to the particle flux it is possible to calculate algebraically the speed of the fast solar wind stream as a function of the delay in the IMF between two spacecraft at known locations, without recourse to a numerical computation of field line growth (which is very demanding in terms of computing time).

The Sun-Wind-ACE IMF system is shown schematically in Figure 11. A single location (i.e. a single field line) is considered. An element of solar wind plasma is emitted from solar location S_w , travels radially along the Sun-Wind line, and subsequently arrives at the Wind spacecraft (P_w), carrying with it the magnetic signature of its source location at the solar surface. During the travel time of the plasma element to P_w , the Sun has rotated for a time period $\Delta T_s (= \Delta T_w + \Delta T_a)$, and released a further element from the same solar location (now at position S_a) which has travelled radially along the Sun-ACE line to position P_a .

$$\Delta T_s = \Delta T_w + \Delta T_a \quad (1)$$

It is assumed: (i) that the magnetic field strength of the solar plasma at the location considered does not significantly change during the rotation from S_w to S_a , and (ii) that the plasma is emitted at the same speed from both locations. These assumptions are considered to be reasonable because the rotation time ΔT_s is only 1268 seconds. (Of course, though plasma is emitted continuously, only those elements relevant to this model are considered.)

The total (correlated) delay in the field (T) between Wind and ACE consists of two components: (i) the delay resulting from solar rotation (ΔT_s), and (ii) that resulting from the difference in the radial distances of Wind and ACE from the Sun (ΔT_2):

$$\Delta T = \Delta T_s + \Delta T_2 \quad (2)$$

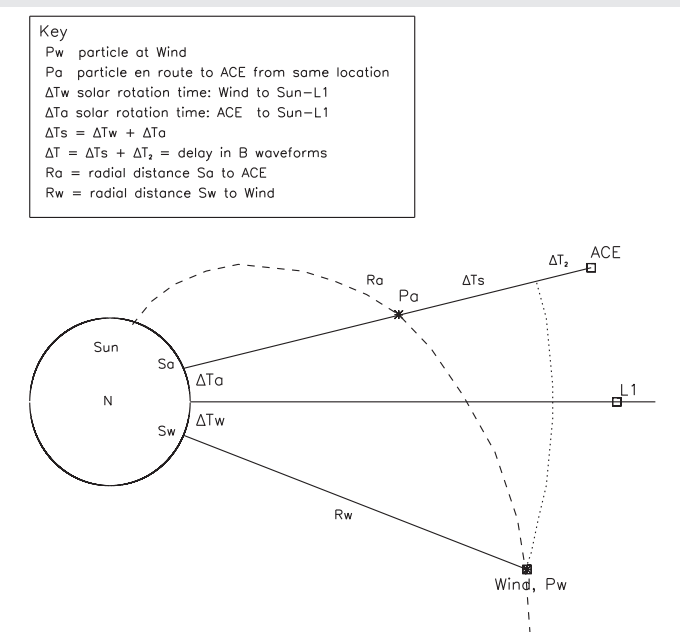


Figure 11: Geometry of Sun, ACE, and Wind, showing particles emitted radially from a single location on the solar surface (and which therefore occupy the same field line).

The solar wind travels the difference in the radial distances between Wind (R_w) and ACE (R_a) at speed V_x in time ΔT_2 :

$$\Delta T_2 = \frac{R_a - R_w}{V_x} \quad (3)$$

Eliminating ΔT_2 , these three equations reduce to the relation:

$$V_x = \frac{R_a - R_w}{\Delta T - \Delta T_s}, \quad (4)$$

or

$$V_x = \frac{\Delta R}{\Delta T - \Delta T_s}. \quad (5)$$

Consequently, the solar wind speed is given by the ratio of the difference in the distances of Wind and ACE from the Sun to the difference between the correlated delay in the IMF from Wind to ACE and the solar rotation time between the Wind and ACE sub-solar locations.

In developing this algebraic model, the only assumptions made about the nature of the solar wind are that over large distances (such as from the Sun to L1): (i) on average, particles in the heliosphere travel in straight radial lines, and (ii) over short time intervals (typically, minutes) particles from the same location on the Sun travel at the same average speed.

Use of the model for the event in question

[It is emphasised that the Sun-to-Earth distance is 100 times that between L1 and Earth, and about 1000 times the distances in the vicinity of the ACE-Wind-L1 system. Consequently, the angle subtended at the Sun-centre by Wind and ACE is only about 0.2° , which justifies the geometric approximations made below].

In equation 5, the value of ΔT when ACE and Wind exhibit peak correlation in B_z ($\Delta T_c = 1610$ seconds from Section 4) is already known for the event in question, but R and ΔT_s have yet to be determined.

Tests proved that, on these distance scales, the spacecraft is close enough to the Sun-Earth line for the Y and Z components of the spacecraft positions to have a negligible effect on the outcome. Consequently, ΔR (the distance between ACE and Wind along the Sun-Earth line) is equal to the distance between the GSE X components of ACE (at 18:00 UT) and Wind (at 17:33 UT, 27 minutes earlier according to the correlation test) on July 1:

$$\Delta R = |X_w - X_a| \quad (6)$$

ΔT_s (the time taken for the locus of a field line on the Sun to rotate from the Sun-Wind line to the Sun-ACE line) is a function of the angle subtended at Sun-centre by Wind and ACE (θ_{wa} , in radians) and the time taken (T_{sun}) for the Sun to complete one rotation (2π radians):

$$\Delta T_s = T_{sun} \cdot \frac{\theta_{wa}}{2\pi} \quad (7)$$

For T_{sun} we adopt the Carrington sidereal rotation time (25.38 days), based on a helio-latitude of 26° . The variable θ_{wa} (radians) is the ratio of the length of the arc of the sector subtended by Wind and ACE at the Sun (Y_{wa}) and the distance from the Sun to the Wind-ACE system (X_{swa}):

$$\theta_{\text{wa}} = \frac{Y_{\text{wa}}}{X_{\text{swa}}} \quad (8)$$

Assuming that it is not an arc but a straight line (reasonable on these scales), Y_{wa} is the sum of the GSE Y components of ACE and Wind:

$$Y_{\text{wa}} = Y_w + Y_a \quad (9)$$

X_{swa} , the mean distance between the Sun and the Wind-ACE system, is the difference between the Sun-Earth distance (X_{se}) and the distance of the Wind-ACE system from Earth:

$$X_{\text{swa}} = X_{\text{se}} - X_{\text{wa}} \quad (10)$$

The distance of the Wind-ACE system from Earth is assumed to be equal to the mean distance of Wind and ACE from Earth (because $X_{\text{wa}} \ll X_{\text{se}}$):

$$X_{\text{wa}} = \frac{X_w + X_a}{2} \quad (11)$$

Finally, X_{se} is the Sun-Earth distance, which is the product of the mean value for 1 AU (1.495978707×10^8 km) and a correction factor (1.016701) based on the fact that Earth's orbit has an eccentricity of 0.0167 [24].

Inserting equations 8 to 11 into equation 7 gives:

$$\Delta T_s = \frac{T_{\text{sun}}(Y_w + Y_a)}{\pi(2X_{\text{se}} - X_w - X_a)} \quad (12)$$

Equations 5, 6, and 12 can then be reduced to a single formula (equation 13) that derives the solar wind speed (V_x) as a function of the delay time from Wind to ACE (ΔT) from a set of fundamental parameters (the values of which are listed in Table 1):

$$V_x = \frac{\pi(X_w - X_a)(2X_{\text{se}} - X_w - X_a)}{\pi\Delta T(2X_{\text{se}} - X_w - X_a) - T_{\text{sun}}(Y_a + Y_w)} \quad (13)$$

Substituting the values for parameters 2 to 7 in Table 1 into equation 13 gives a function of the form $V_x = f(\Delta T)$ which is plotted in Figure 12a. The dotted lines in the figure show the specific case of $V_c = f(\Delta T_c)$ for $\Delta T_c = 1610$ s (parameter 1 in Table 1), giving a solar wind speed (V_c) of 438.7 km.s^{-1} , a value which agrees very closely with the speed measured by Wind at 17:33 UT on July 1 (436.6 km.s^{-1}), and that measured by ACE at 18:00 UT (437.3 km.s^{-1}). This speed is within the boundary between the slow and fast solar wind ($400 - 450 \text{ km.s}^{-1}$).

Discussion

Error analysis

The total error in V_x is a function of the individual errors in the fundamental parameters listed in Table 1. As regards the

error in ΔT_c (parameter 1), correlation tests between the Wind and ACE 1-second B_z data revealed that a distinct delay (1610 seconds) can be derived from the period of maximum activity (centred at 18:00 UT on July 1) in which B_z is most structured. The correlation coefficient remains almost constant (0.87 to 0.90) when the duration of this period varies from 3 to 6 (± 1.5 to 3.0) hours. This is considered to be a robust result for which the delay can be assumed to be accurate to within 1 second. As the derivative of V_x shows (Figure 12b), $dV_x/d(\Delta T)$ is only -1.28 km.s^{-2} , which means that V_x is accurate to within $\pm 1 \text{ km.s}^{-1}$.

However, the errors in ΔR and ΔT_s must also be taken into account, which are dependent on parameters 2 to 7 in Table 1. The Sun-Earth distance (X_{se}) has been corrected for Earth's orbit eccentricity on July 1 2005 by interpolation of a table of aphelion and perihelion values (the aphelion being on July 5), so the error is assumed to be negligible. The Carrington sidereal solar rotation time (T_{sun}), consistent with the latitude of periodic solar activity, is a well-known parameter that has an uncertainty of no more than ± 0.01 days (209 seconds). This

Table 1: Fundamental parameters required by equation 13.

| | Parameter | Symbol | Value | Units | Uncertainty |
|---|---|------------------|----------------------|-------|-------------|
| 1 | Wind-ACE B_z delay time | ΔT_c | 1610 | secs | negligible |
| 2 | Sun-Earth distance | X_{se} | $1.51993\text{e}+08$ | km | negligible |
| 3 | Solar sidereal rotation period (Carrington) | T_{sun} | 25.38 | days | ± 0.01 |
| 4 | ACE GSE x component | X_a | 1510923 | km | ± 40 |
| 5 | ACE GSE y component | Y_a | 266957 | km | ± 40 |
| 6 | Wind GSE x component | X_w | 1660791 | km | ± 20 |
| 7 | Wind GSE y component | Y_w | 279663 | km | ± 20 |

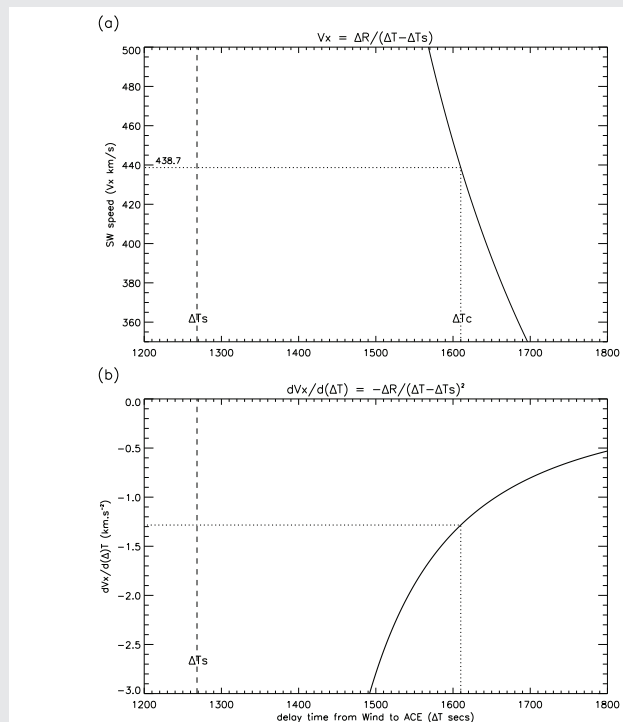


Figure 12: (a) Results of the algebraic model for the parameter values in Table 1. (b) Derivative, $dV_x/d(\Delta T)$. (Error bars are too small to be discernible on these plots.)

also gives an accuracy for V_x to within $\pm 1 \text{ km.s}^{-1}$. The errors in the X and Y GSE positions of Wind and ACE, provided by NASA GSFC, are within ± 20 and 40 km (respectively). Tests show that the effect of this uncertainty is negligible.

To summarise, the combined effect of the errors in Table 1 is that, using this method, the deduced solar wind speed is accurate to within $\pm 1 \text{ km.s}^{-1}$ overall. When plotted, this value is too small to discern in Figure 12.

Limits of applicability

To assess the efficacy of this method for other spacecraft geometries it is necessary to consider their proximity in relation to the response of equation 5 when ΔT_s and ΔR vary, and to consider how these variations affect not only the function itself but also the gradient $dV_x / d(\Delta T)$ (which determines the sensitivity of V_x with respect to ΔT). It is the gradient that is the significant factor in this discussion.

Varying ΔT_s (the angular separation of the spacecraft at the Sun-centre) only translates the curve and its asymptote on the abscissa in Figure 12. This will have no effect on the accuracy of the deduced speed with respect to ΔT . Consequently, there are no limits on the angular separation of the two spacecraft, except for the reduction in waveform coherence which is in turn affected by event intensity (discussed below).

The effect of ΔR on the accuracy of the deduced speed is more significant. Figure 13 shows how $dV_x / d(\Delta T)$ varies with speed, for a range of values of ΔR from 120000 to 600000 km. The approximate limits of the fast solar wind ($450 - 900 \text{ km.s}^{-1}$) are marked by dashed lines, and the gradient values at -1 , -2 , -4 , and -8 km.s^{-2} are marked by dotted lines. The variation in the accuracy of the deduced speed over a range of values of ΔR can now be investigated.

For $\Delta T = \pm 1 \text{ s}$, if an accuracy of 1 km.s^{-1} is required, then at a separation of 600000 km (curve 1 in Figure 13) the maximum speed that can be deduced is 770 km.s^{-1} (though for slower speeds even higher accuracy is attainable). At half the separation (curve 2) only speeds up to 550 km.s^{-1} can be deduced to 1 km.s^{-1} accuracy. As the separation decreases, this trend continues, so that in the case of curve 5 (separation 120000 km) the solar wind speed must be as low as 350 km.s^{-1} (which is clearly in the slow domain where IMF structure is lacking and therefore sufficient correlation is unlikely). For a lower accuracy, the speed constraint can be relaxed. For example, if 4 km.s^{-1} is acceptable, then curve 3 shows that a maximum solar wind speed of 900 km.s^{-1} can be deduced at a separation of 200000 km, higher speeds requiring greater separation (though speeds rarely exceed 1000 km.s^{-1}).

The implications of Figure 13 are summarised in Table 2. This shows that, for the highest accuracy (1.0 km.s^{-1}), a separation of over 600000 km is required to cover fast solar wind speeds up to 770 km.s^{-1} . However, if the accuracy constraint is relaxed to 8.0 km.s^{-1} the full range of fast solar wind speeds can be accommodated at a separation as low as 120000 km.

There is, however, another important factor: the coherence of B_z will diminish with increasing spacecraft separation,

reducing the correlation coefficient, and therefore the accuracy of ΔT_s . Richardson and Paularena [25] used IMF data from multiple spacecraft to determine IMF correlation coefficients for more than 4000 6-hour periods from 1997 to 1998 (irrespective of solar wind speed). As X separations increased from 0 to $280 R_e$ ($1.78 \times 10^6 \text{ km}$) the correlation coefficients decreased by ≤ 0.1 . There was much more variation of the correlation coefficients with spacecraft separation in the YZ plane, with a significant decrease for separations greater than $45 R_e$ ($2.87 \times 10^5 \text{ km}$).

Weygand, et al. [26] used simultaneous multi-point measurements of the IMF from 11 spacecraft to determine the correlation scale of the solar wind as a function of the mean magnetic field direction and solar wind speed, involving a total of about 4400 cross-correlations. At speeds $\leq 600 \text{ km.s}^{-1}$ the correlation coefficient decreased from 1.0 (at zero separation) to 0.4 in the X direction and 0.2 in the YZ plane (at $2.0 \times 10^6 \text{ km}$ separation). At speeds $> 600 \text{ km.s}^{-1}$, the correlation coefficient decreased to 0.2 in the X direction (the YZ value being the same).

These results suggest that there is likely to be a separation limit in both the X and YZ directions beyond which the coherence of B_z reduces to such an extent that the correlation is too weak for equation 5 to give a useful result. However, this limit is difficult to specify because it will also be dependent on the amount of structure present in the IMF, which will in turn be dependent on the intensity of the event under analysis (related to the solar wind speed). For example, it is likely that an energetic CME would provide sufficient structure to

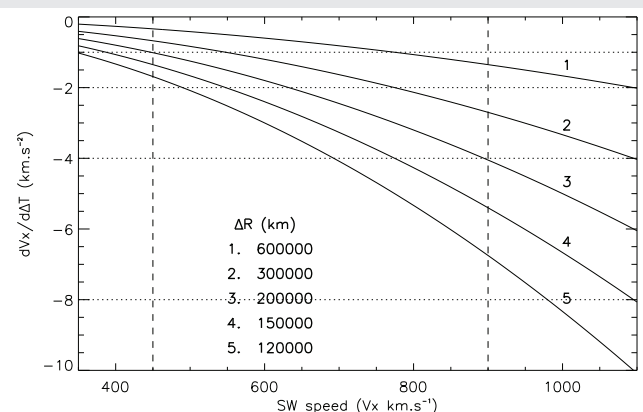


Figure 13: Variation of $dV_x / d(\Delta T)$ with V_x (ΔR increasing from 120000 to 600000 km, and ΔT_s fixed at 1268 s). The dashed lines mark the nominal limits of the fast solar wind.

Table 2: Maximum solar wind speed that can be deduced in equation 5, for variations in accuracy and spacecraft separation (from Figure 13).

| Accuracy in deduced | Maximum solar wind speed (km.s^{-1}) | | | | |
|--|---|--------|--------|--------|--------|
| V_x for $\Delta T = \pm 1 \text{ s}$ | for spacecraft separation (ΔR km) | | | | |
| ($\pm \text{km.s}^{-1}$) | 120000 | 150000 | 200000 | 300000 | 600000 |
| 1.0 | 350 | 380 | 450 | 550 | 770 |
| 2.0 | 490 | 550 | 640 | 770 | 1100 |
| 4.0 | 690 | 770 | 900 | 1100 | >1100 |
| 8.0 | 975 | 1100 | >1100 | >1100 | >1100 |

allow for greater separations than those herein, though this conjecture has yet to be tested.

(To determine the effect of variations in coherence a statistical approach is required involving a range of selected events with varying levels of activity. A study is in progress that will address this subject.)

Slow solar wind

The same correlation tests carried out on a period of slow solar wind on June 30 centred at 18:00 UT gave poor results: correlation coefficients from 0.33 to 0.55, with peaks barely above the background resulting in extreme, random delays (probably because of insufficient coherence). Consequently, it is concluded that this method is unsuitable for use on the slow solar wind.

Parker spiral fluctuations

The model developed in Section 5 assumes that the solar wind follows a simple Parker spiral structure: fluctuations due to turbulence or electromagnetic instabilities have not been taken into account [27]. Turbulence refers to a class of phenomena that characteristically occurs in fluids and plasmas when non-linear effects are dominant. Non-linearity creates complexity, involvement of many degrees of freedom, and a lack of predictability [28], making the true form of the Parker spiral intrinsically statistical [29].

Analysis of heliospheric magnetic field observations suggests that the majority of the fluctuations are transverse, varying in the direction normal to the background magnetic field. Such turbulence will cause the field lines to meander across the mean field direction [30].

Considering that the model assumes the existence of a non-turbulent Parker spiral, the close agreement between the observed and modelled solar wind speeds ($< 2 \text{ km.s}^{-1}$, or 0.4%) is quite remarkable.

Use of other spacecraft

Though Wind and ACE have been used in this study, any pair of current or future spacecraft that (1) are located in deep space (i.e. not within planetary magnetospheres), (2) comply with the limits of applicability defined in Section 7.2, and (3) carry onboard magnetometers, can potentially be used to determine the speed of the fast solar wind using the method defined herein. Examples of current missions are Ulysses and STEREO, plus the more recent Parker Solar Probe and Solar Orbiter. However, given that these spacecraft are at various and changing locations within the heliosphere, it is very unlikely that any pair will be sufficiently proximate to satisfy condition 2 (the limits of applicability, Section 7.2). Only Wind and ACE, located in the vicinity of L1, are suitable candidates (though future missions may comply).

Conclusion

An algebraic model has been presented with which the speed of a fast solar wind stream can be deduced from the

interplanetary magnetic field using independent observations of B_z by two spacecraft at different locations. A running cross-correlation using ± 3 hours of B_z data at the mid-point of the active period gave a distinct peak with a correlation coefficient of 0.88 and a delay of 1610 seconds. Substituting the cross-correlated delay into the algebraic model gives a solar wind speed of 438.7 km.s^{-1} , a result which agrees with the measured speed at Wind and ACE to within 0.4%.

Though this result is based on a specific case, the model can, in principle, be applied to any two spacecraft that comply with the following conditions:

1. The smaller the radial separation of the two spacecraft, the greater the uncertainty in the deduced speed (becoming uncertain at less than about 120000 km, and insoluble at zero separation),
2. The greater the radial separation of the two spacecraft, the less will B_z remain sufficiently coherent to give an adequate correlation (though compensated by (4) to some extent),
3. There are no constraints on angular separation, even if the spacecraft is on the same helio-meridian (though the coherence limit in (2) still applies),
4. The more intense the activity (e.g. energetic CMEs) the more structure is likely to be present in the IMF and the more likely is an adequate correlation with increased spacecraft separation (both angular and radial).

Given these conditions, the method provides a means of determining the speed of the solar wind particle flux using measurements of the flux density of the magnetic field. This is useful in situations when particle data is not available, such as in cases of instrument failure, or sensor saturation during very energetic CME events, when magnetometers continue to function. However, given the requirement that a pair of spacecraft with the above separation constraints are required, it is accepted that such occasions will inevitably be infrequent.

Tests have shown that there is insufficient coherent structure in the slow solar wind for this method to be applicable.

Acknowledgement

The groundwork for this paper originated during the author's PhD studies, supervised by Dr. B.J.I. Bromage (now deceased). Though not involved with the data analysis and preparation of this paper, Dr. Bromage was instrumental in the early research and is hereby given full recognition for her supervision and scientific contribution.

The authors wish to thank NASA GSFC for the provision of the ACE and Wind data used in this study.

References

1. Chapman S. On the Origin of the Aurora Polaris. *Phys Rev.* 1928;32(6):993-995. Available from: <https://journals.aps.org/pr/abstract/10.1103/PhysRev.32.993>

2. Chapman S, Ferraro VCA. The electrical state of solar streams of corpuscles. *Mon Not R Astron Soc.* 1929;89:470. Available from: <https://doi.org/10.1093/mnras/89.5.470>
3. Ferraro VCA. A new theory of magnetic storms: a critical survey. *The Observatory.* 1933;56:253-259. Available from: <https://adsabs.harvard.edu/full/1933Obs....56..253F>
4. Biermann L. Kometenschweife und solare Korpuskularstrahlung. *Z Astrophys.* 1951;29:274-286. Available from: <https://ui.adsabs.harvard.edu/abs/1951ZA.....29..274B/abstract>
5. Parker EN. Dynamics of the Interplanetary Gas and Magnetic Fields. *Astrophys J.* 1958;128:664. Available from: https://ui.adsabs.harvard.edu/link_gateway/1958ApJ...128..664P/doi:10.1086/146579
6. Chapman S, Aller LH. Diffusion in the sun. *Astron J.* 1959;64:126. Available from: https://ui.adsabs.harvard.edu/link_gateway/1959AJ....64..126C/doi:10.1086/107896
7. Snyder CW. Mariner Solar Wind Measurement. In: Hess WN, editor. *The Physics of Solar Flares. Proceedings of the AAS-NASA Symposium held 28-30 October, 1963 at the Goddard Space Flight Center, Greenbelt, MD.* Washington DC: National Aeronautics and Space Administration, Science and Technical Information Division. 1964;273.
8. Balogh A, Beek TJ, Forsyth RJ, Hedgecock PC, Marquedant RJ, Smith EJ, Southwood DJ, Tsurutani BT. The magnetic field investigation on the ULYSSES mission - Instrumentation and preliminary scientific results. *Astron Astrophys Suppl Ser.* 1992;92(2):221-236. Available from: <https://ui.adsabs.harvard.edu/abs/1992A%26AS...92..221B/abstract>
9. Cranmer S. Coronal holes and the high-speed solar wind. *Space Sci Rev.* 2002;101:229-294. Available from: <https://citeseerx.ist.psu.edu/document?repid=rep1&type=pdf&doi=d0b02f0daaa11be898877058a615ed07d0c3884>
10. Cranmer S. Coronal holes. *Living Rev Sol Phys.* 2009;6(3). Available from: <https://link.springer.com/article/10.12942/lrsp-2009-3>
11. Lukianova R, Holappa L, Mursula K. Centennial evolution of monthly solar wind speeds: Fastest monthly solar wind speeds from long-duration coronal holes. *J Geophys Res Space Physics.* 2017;122(3):2740-2747. Available from: <https://doi.org/10.1002/2016JA023683>
12. Einaudi G, Boncinelli P, Dahlburg RB, Dahlburg JT, Karpen J. Formation of the slow solar wind in a coronal streamer. *J Geophys Res.* 1999;104(A1):521-534. Available from: <https://agupubs.onlinelibrary.wiley.com/doi/pdf/10.1029/98JA02394>
13. Ofman L. The origin of the slow solar wind in coronal streamers. *Adv Space Res.* 2004;33(5):681-688. Available from: <https://www.sidc.be/users/evanob/Literature/Papers/Solar%20Physics/2004%20Ofman%20Origin%20of%20slow%20SW%20in%20streamers.pdf>
14. Bravo S, Stewart GA. Fast and Slow Wind from Solar Coronal Holes. *Astrophys J.* 1997;489:992. Available from: <https://iopscience.iop.org/article/10.1086/304789>
15. Sulistiani S, Herdiwijaya D. Solar coronal holes and their geo-effectiveness. *J Phys Conf Ser.* 2019;1127(1):012052. Available from: <http://dx.doi.org/10.1088/1742-6596/1127/1/012052>
16. Verbanac G, Vrsnak B, Veronig A, Temmer M. Equatorial coronal holes, solar wind high-speed streams, and their geoeffectiveness. *Astron Astrophys.* 2011;526(A20):1-13. Available from: <https://doi.org/10.1051/0004-6361/201014617>
17. Heber B, Sanderson TR, Zhang M. Co-rotating interaction regions. *Adv Space Res.* 1999;23(3):567-579. Available from: <https://ui.adsabs.harvard.edu/abs/1999AdSpR...23..567H/abstract>
18. Hajra R, Sunny JV. Corotating interaction regions during solar cycle 24: A study on characteristics and geoeffectiveness. *Solar Phys.* 2022;297:30. Available from: <http://dx.doi.org/10.1007/s11207-022-01962-1>
19. Del Zanna G, Bromage BJI. The Elephant's Trunk: Spectroscopic diagnostics applied to SOHO/CDS observations of the August 1996 equatorial coronal hole. *J Geophys Res.* 1999;104(A5):9753-9766. Available from: <https://ui.adsabs.harvard.edu/abs/1999JGR...104.9753D/abstract>
20. McComas DJ, Bame SJ, Barker P, Feldman WC, Phillips JL, Riley P, et al. Solar Wind Electron Proton Alpha Monitor (SWEPAM) for the Advanced Composition Explorer. *Space Sci Rev.* 1998;86(1/4):563-612. Available from: <https://link.springer.com/article/10.1023/A:1005040232597>
21. Smith CW, L'Heureux J, Ness NF, Acuña MH, Burlaga LF, Scheifele J. The ACE Magnetic Fields Experiment. *Space Sci Rev.* 1998;86(1/4):613-632. Available from: <https://ui.adsabs.harvard.edu/abs/1998SSRv...86..613S/abstract>
22. Ogilvie KW, Chornay DJ, Fritzenreiter RJ, Hunsaker F, Keller J, Lobell J, et al. SWE, A Comprehensive Plasma Instrument for the Wind Spacecraft. *Space Sci Rev.* 1995;71(1-4):55-77. Available from: <https://link.springer.com/article/10.1007/BF00751326>
23. Lepping RP, Acuña MH, Burlaga LF, Farrell WM, Slavin JA, Schatten KH, et al. The Wind Magnetic Field Investigation. *Space Sci Rev.* 1995;71(1-4):207-229. Available from: <https://link.springer.com/article/10.1007/BF00751330>
24. Espenak F. Earth at Perihelion and Aphelion: 2001 to 2100 [Internet]. Fred Espenak. Available from: <http://www.astropixels.com/ephemeris/perap2001.html>
25. Richardson JD, Paularena KI. Plasma and Magnetic Field Correlations in the Solar Wind. *J Geophys Res.* 2001;106(A1):239-251. Available from: <https://doi.org/10.1029/2000JA000071>
26. Weygand JM, Mattheus WH, Dasso S, Kivelson MG. Correlation and Taylor scale variability in the interplanetary magnetic field fluctuations as a function of solar wind speed. *J Geophys Res.* 2011;116:A08102. Available from: <https://doi.org/10.1029/2011JA016621>
27. Bian NH, Li G. Transport of Solar Energetic Particles along Stochastic Parker Spirals. *Astrophys J.* 2022;924:120. Available from: <https://iopscience.iop.org/article/10.3847/1538-4357/ac2fab/meta>
28. Raouafi NE, Matteini L, Squire J, Badman ST, Velli M, Klein KG, et al. Parker Solar Probe: Four Years of Discoveries at Solar Cycle Minimum. *Space Sci Rev.* 2023;219:8. Available from: <https://link.springer.com/article/10.1007/s11214-023-00952-4>
29. Bian NH, Li G. Stochastic Parker Spirals in the Solar Wind. *Astrophys J.* 2021;908:45. Available from: <https://ui.adsabs.harvard.edu/abs/2021ApJ...908...45B/abstract>
30. Laitinen T, Dalla S, Waterfall COG, Hutchinson A. An Analytical Model of Turbulence in Parker Spiral Geometry and Associated Magnetic Field Line Lengths. *Astrophys J.* 2023;943:108. Available from: <https://iopscience.iop.org/article/10.3847/1538-4357/aca892>